Energy & Environmental Science

PAPER

Exceptional long-life performance of lithium-ion batteries using ionic liquid-based electrolytes†

Cite this: DOI: 10.1039/c6ee01295g

Giuseppe Antonio Elia,‡[a] Ulderico Ulissi,‡[bc] Sangsik Jeong,[bc] Stefano Passerini*[bc] and Josef Hassoun*[d]

Received 4th May 2016,
Accepted 15th August 2016

DOI: 10.1039/c6ee01295g

www.rsc.org/ees

Advanced ionic liquid-based electrolytes are herein characterized for application in high performance lithium-ion batteries. The electrolytes based on either *N*-butyl-*N*-methyl-pyrrolidinium bis(trifluoromethanesulfonyl)imide ($Pyr_{14}TFSI$), *N*-butyl-*N*-methyl-pyrrolidinium bis(fluoro-sulfonyl)imide ($Pyr_{14}FSI$), *N*-methoxy-ethyl-*N*-methylpyrrolidinium bis(trifluoromethane-sulfonyl)imide ($Pyr_{12O1}TFSI$) or *N*-*N*-diethyl-*N*-methyl-*N*-(2-methoxyethyl)ammonium bis(trifluoromethanesulfonyl)imide (DEMETFSI) ionic liquids and lithium bis(trifluoromethanesulfonyl)imide (LiTFSI) are fully characterized in terms of ionic conductivity, viscosity, electrochemical properties and lithium-interphase stability. All IL-based electrolytes reveal suitable characteristics for application in batteries. Lithium half-cells, employing a $LiFePO_4$ polyanionic cathode, show remarkable performance. In particular, relevant efficiency and rate-capability are observed for the $Py_{14}FSI$–LiTFSI electrolyte, which is further characterized for application in a lithium-ion battery composed of the alloying Sn–C nanocomposite anode and $LiFePO_4$ cathode. The IL-based full cell delivers a maximum reversible capacity of about 160 mA h g^{-1} (*versus* cathode weight) at a working voltage of about 3 V, corresponding to an estimated practical energy of about 160 W h kg^{-1}. The cell evidences outstanding electrochemical cycle life, *i.e.*, extended over 2000 cycles without signs of decay, and satisfactory rate capability. This performance together with the high safety provided by the IL-electrolyte, olivine-structure cathode and Li-alloying anode, makes this cell chemistry well suited for application in new-generation electric and electronic devices.

Broader context

This new lithium ion battery is composed of a *N*-butyl-*N*-methyl-pyrrolidinium bis(fluoro-sulfonyl)imide ($Pyr_{14}FSI$)–lithium bis(trifluoromethanesulfonyl)imide (LiTFSI) IL-electrolyte, Sn–C nanocomposite Li-alloying anode and $LiFePO_4$ olivine cathode. The non-volatile, poorly-flammable electrolyte is advantageously selected based on a comparative study of various ILs differing by the chemical structure, while the anode and cathode are considered very promising electrodes in terms of cycle life, interface stability, energy content and rate capability. The battery delivers a reversible capacity of about 160 mA h g^{-1} at a working voltage of about 3 V, and an estimated practical energy of about 160 W h kg^{-1} for over 2000 cycles. Such outstanding cycle life, high efficiency and rate capability as well as the expected low environmental impact and high safety content suggest the application of the studied battery in new-generation electric and electronic devices.

Introduction

High-energy, light lithium-ion batteries (LIBs) are nowadays the power source of choice for several classes of portable electronic devices[1] and the most appealing candidates for application in electric vehicles (EVs).[2,3] However, commercial LIBs, employing a graphitic carbon anode, carbonate-based organic electrolyte and lithiated transition metal oxide cathode,[4] do not offer the high safety required in the EV field. The possible degradation of the solid electrolyte interphase (SEI) layer at the graphite anode, leading to flammable gaseous emission by continuous electrolyte decomposition[5,6] and oxygen evolution by overheating of the charged cathode, are just some examples of the few events leading to unsafe cell conditions.[7] Furthermore, the presence of the highly flammable organic electrolyte renders the present LIB technology prone to a catastrophic event called "thermal runaway".[7–10]

[a] *Technische Universität Berlin, Research Center of Microperipheric Technologies, Gustav-Meyer-Allee 25, 13355 Berlin, Germany*
[b] *Helmholtz Institute Ulm (HIU), Helmholtzstrasse 11, 89081 Ulm, Germany*
[c] *Karlsruhe Institute of Technology (KIT), P.O. Box 3640, 76021 Karlsruhe, Germany. E-mail: Stefano.passerini@kit.edu*
[d] *Department of Chemical and Pharmaceutical Sciences, University of Ferrara, Via Fossato di Mortara, 44121, Ferrara, Italy. E-mail: jusef.hassoun@unife.it*

† Electronic supplementary information (ESI) available. See DOI: 10.1039/c6ee01295g

‡ These authors equally contributed.

Several efforts aiming at the development of alternative systems characterized by new chemistries appear to be of crucial importance in order to allow the deployment of LIBs in appealing markets such as large stationary storage and electromobility. Among the cathode materials, olivine-structure electrodes, such as carbon coated $LiFePO_4$,[11] reveal very promising features in terms of remarkable intrinsic safety due to the extended stability of the polyanionic framework involving $-PO_4$ bonds.[12] Li-alloying electrodes are considered as very promising anode materials, alternative to graphite. Silicon and tin exchange up to 4.4 equivalents of lithium, with theoretical specific capacities of 4200 mA h g^{-1} and 990 mA h g^{-1}, respectively, *i.e.*, a much higher value compared to graphite (372 mA h g^{-1}).[13] A further attractive characteristic of the Li-alloy anodes, suitable for application in advanced lithium ion batteries, is represented by a working voltage slightly higher than that of graphite, thus mitigating the reductive electrolyte decomposition and possible lithium plating and contributing to improved cell safety.[14] Tin and silicon are also considered non-toxic and environmentally compatible,[15,16] peculiarities that suggest their application in green energy storage systems.[17] However, this class of electrode materials suffers from a huge volume expansion during the electrochemical process with lithium leading to the electrode pulverization and a huge capacity fading.[18,19] This issue has been mitigated[18] by including nanoparticles of the active material in a buffer matrix, such as carbon or an inactive metal, to form nanocomposites[20–32] characterized by improved cycle life and electrochemical performances in batteries.

Besides the development of novel electrode materials, several efforts have been devoted to the development of alternative electrolytes characterized by increased safety. The aforementioned risk related to the thermal runaway can be effectively greatly mitigated by employing a thermally stable electrolyte that may actually lead to a remarkable improvement of the safety level of the devices. In this respect, room temperature ionic liquids (RTILs, *i.e.*, molten salts at room temperature) appear to be the most appealing alternatives to the conventional organic electrolytes.[33,34] RTILs can be engineered by changing their structure, thus tailoring their properties, in order to contemporarily meet various important needs such as high ionic conductivity, interfacial and electrochemical stabilities as well as thermal stability and low-flammability.[35,36] These features allows the realization of safer electrochemical storage devices such as supercapacitors,[37–39] batteries[40–53] and solar cells.[54]

Herein, mixtures of *N*-butyl-*N*-methylpyrrolidinium bis(trifluoromethanesulfonyl)imide (Pyr_{14}TFSI), *N*-butyl-*N*-methyl-pyrrolidinium bis(fluorosulfonyl)imide (Pyr_{14}FSI), *N*-methoxy-ethyl-*N*-methyl-pyrrolidinium bis(trifluoromethanesulfonyl)imide (Pyr_{12O1}TFSI) or *N*-*N*-diethyl-*N*-methyl-*N*-(2-methoxyethyl)ammonium bis(trifluoromethanesulfonyl)imide (DEMETFSI)[55–58] with lithium bis(trifluoromethanesulfonyl)imide (LiTFSI) are comparatively evaluated for application as electrolytes in Li-ion batteries (see structural details in Fig. S1 of the ESI†). The Pyr_{14}TFSI-based electrolyte is characterized by remarkable electrochemical stability in a lithium cell and by suitable ionic conductivity.[50,51,59] However, the main issue of this excellent electrolyte is represented by its high viscosity, which limits the electrochemical performance at high currents. The anion and cation structures can greatly influence the electrochemical proprieties of the IL electrolyte.[60] Pyr_{14}FSI, differing from Pyr_{14}TFSI by the anion structure (Fig. S1d of ESI†), is indeed characterized by a lower viscosity but higher chemical reactivity due to the S–F bonds. Hence, electrolytes based on Pyr_{14}FSI show higher ionic conductivity and enhanced SEI film forming ability compared to those based on Pyr_{14}TFSI.[61,62] A recent study has shown that Li/$LiCoO_2$ batteries employing FSI-based electrolytes are characterized by a greatly improved rate capability compared to those employing TFSI-based ILs.[63] Besides the anion, the cation can also be modified in order to obtain enhanced characteristics. The substitution of one carbon with an oxygen atom in the alkyl side chain of Pyr_{14}, leading to Pyr_{12O1}, results in the higher flexibility of the side chain as a result of the ether bond formed (Fig. S1b of ESI†). The Pyr_{12O1}TFSI-based electrolyte has consequently lower viscosity and higher conductivity than the Pyr_{14}TFSI-based one.[64] Recent studies suggested suitable electrochemical performance in lithium batteries with ILs formed by aliphatic quaternary ammonium, such as DEME,[65,66] even comparable to pyrrolidinium-based ILs.[67] Our work focuses on the evaluation of the electrochemical characteristics of ionic liquid electrolytes differing by the structure in lithium batteries. The electrolyte showing the best properties, namely Pyr_{14}FSI–LiTFSI, is studied in a full lithium-ion cell employing the LFP cathode and nanostructured Sn–C anode.[68] The results obtained highlight the outstanding cycle life, with capacity retention close to 100% over 2000 cycles, rate capability extending up to 500 mA g^{-1} and energy content as high as 480 W h kg^{-1} (referred to the cathode weight only). These performances, rarely reported in the literature for lithium ion cells employing ionic liquid-based electrolytes,[59] have been further highlighted by impedance spectroscopy (EIS) and scanning electron microscopy (SEM) studies.

Experimental

The electrolytes were prepared by mixing in 0.2 mol of LiTFSI (3M, battery grade) per kg of either Pyr_{14}TFSI, Pyr_{14}FSI, Pyr_{12O1}TFSI or DEMETFSI in an argon filled glove box (MBRAUN), with oxygen and water contents lower than 1 ppm. The electrolytes were dried under vacuum for 24 hours at 120 °C (Pyr_{14}TFSI–LiTFSI), 60 °C (Pyr_{14}FSI–LiTFSI), 60 °C (Pyr_{12O1}TFSI–LiTFSI) and 80 °C (DEMETFSI–LiTFSI) until the water content was reduced to less than 5 ppm (detection limit) as determined by Karl Fischer titration. The drying conditions have been chosen considering the thermal stability of each IL-based electrolyte, in order to avoid possible decomposition promoted by the presence of water traces during the initial stages of the drying process.[69,70] The lithium salt concentration in the ionic liquid-based electrolytes, *i.e.*, 0.2 mol kg^{-1}, has been demonstrated as the optimal compromise allowing a high lithium ion conductivity and charge transport and simultaneously avoiding an undesired viscosity increase, thus leading to satisfactory cell

performance in terms of delivered capacity, low polarization and high rate capability.[69,70] The electrolyte conductivity Arrhenius plots were obtained by electrochemical impedance spectroscopy (EIS, Mmates-Biologic) by means of sealed Pt-black/Pt-black cells (Mmates) with a K value of 1 cm^{-1}, using a Peltier system for cooling/heating as temperature control. The reported conductivity plots are obtained upon heating, after eighteen hours of aging at −40 °C, with an increment of 5 °C per hour. The cell constant was confirmed using the standard 0.1 M KCl water solution (Fluka). The viscosity of the electrolytes was evaluated at various temperatures in a dry room environment by means of an Anton-Paar Physica MCR102 rheometer, applying constant shear rates, and using a Peltier system for cooling/heating. The viscosity plots are obtained upon heating, after six hours of aging at −40 °C, with an increment of 10 °C per hour. The cycling stability of the lithium metal in the IL-based electrolytes was evaluated by continuous stripping/deposition tests on symmetrical Li/Li cells in coin cell cases, reversing the current (0.1 mA cm^{-2}) every one hour.

The electrochemical anodic stability of the electrolytes was evaluated by linear sweep voltammetry (scan rate of 0.1 mV s^{-1}) using a composite carbon (Super C65, Imerys) coated on aluminum foil as the working electrode. The current *versus* time plots for the anodic stability were obtained by applying increasing voltage steps of 0.1 V (each lasting one hour). The cathodic stability was determined by cyclic voltammetry in the 0.01–2 V potential range at a 0.1 mV s^{-1} scan rate employing a composite carbon electrode (Super C65, Imerys) coated on copper foil as the working electrode. These experiments were performed on Swagelok-type cells with lithium metal as the reference electrode. All the electrochemical tests were carried out at 40 °C in thermostatic climatic chambers with a possible deviation of ±1 °C.

Composite electrodes were prepared by the doctor-blade technique, coating a slurry composed of C-NERGY Super C65 (Imerys), PVDF (6020 Solef, Solvay) and the active materials ($LiFePO_4$, LFP, or tin–carbon composite, Sn–C) in a 1 : 1 : 8 weight ratio, dispersed in *N*-methyl-2-pyrrolidinone (NMP, Aldrich 99.9%) and cast either on aluminum (LFP) or copper (Sn–C) foils. After drying, the coated foils were punched into disk-shaped electrodes having a diameter of 14 mm (LFP) or 16 mm (Sn–C), the residual solvent and water traces were removed under vacuum at 110 °C overnight. The electrode mass loading was about 2–3 mg cm^{-2} for Sn–C and about 4–5 mg cm^{-2} for LFP. Specific capacity and currents were evaluated taking into account a maximum error of 5% mostly due to the uncertainty in the electrode loadings (±0.1 mg). The Sn–C nanocomposite (Sn/C weight ratio of approximately 40 : 60) was prepared as previously described,[71] while the LFP preparation was reported in a previous work.[72] The theoretical specific capacity of the nanocomposite material was calculated to be approximately 440 mA h g^{-1} at room temperature, assuming contributions of tin and carbon of 380 and 60 mA h g^{-1}, respectively.

The electrochemical characterization for lithium half cells was performed using stainless steel 2032 coin cells, with lithium metal as the counter electrode, a sheet of Whatman glass fiber GF/A soaked by the electrolyte as the separator and either LFP or pre-activated Sn–C as the working electrode. Prior to half and full cell assembling, the Sn–C anode was pre-activated by placing the electrode in contact with a Li foil wetted by a LP30 solution to compensate for the irreversible capacity shown by this material upon the 1st lithiation[68,73] and allow the formation of a stable SEI layer at the anode surface, as already demonstrated by previous works[73,74] and the results herein reported. We have attempted the same pre-activation procedure by directly pressing the anode in the presence of the IL-based electrolyte instead of the conventional one. However, this resulted in a mechanical degradation of the anode, avoiding the proper pre-activation and SEI film formation. The cycling tests of Li/IL-based electrolyte/LFP cells were carried out applying increasing specific currents (from 25 to 250 mA g^{-1}) in the voltage range 2.2–4 V, while those of Li/Pyr_{14}FSI–LiTFSI/Sn–C cells were performed applying increasing specific currents from 25 mA g^{-1} to 200 mA g^{-1} in the voltage range 0.01–2 V. The Sn–C/Pyr_{14}FSI–LiTFSI/LFP cell was tested in the voltage range 2–3.8 V at specific currents increasing from 25 to 250 mA g^{-1}, while a fingerprint test was performed employing a specific current of 500 mA g^{-1}, which was lowered to 25 mA g^{-1} for three cycles every 45 cycles. All galvanostatic cycling tests were carried out at 40 °C in a thermostatic climatic chamber (with a possible deviation of ±1 °C) using a Maccor 4000 Battery Test System. The specific current and the specific capacity are referred to the cathode (LFP) weight. The impedance measurements were performed within the frequency range from 200 kHz to 10 mHz applying a 10 mV sinusoidal amplitude using a VMP3 potentiostat/galvanostat/EIS (Bio-Logic).

The *ex situ* morphological characterization was performed using field emission scanning electron microscopy (SEM, Zeiss LEO1550VP Gemini). Prior to the SEM analyses, the studied electrodes were rinsed using dimethyl carbonate (DMC) in order to remove residual electrolyte components.

Results and discussion

The electrolyte; conductivities and viscosities are reported in Fig. 1. The Arrhenius plot in Fig. 1a shows that Pyr_{14}FSI–LiTFSI (black dots) is characterized by the highest ionic conductivity, with the values ranging from 15 mS cm^{-1} at 60 °C to 0.3 mS cm^{-1} at −30 °C. Progressively decreasing conductivity values are shown by Pyr_{12O1}TFSI–LiTFSI (blue dots, 10 mS cm^{-1} at 60 °C and 0.05 mS cm^{-1} at −30 °C), Pyr_{14}TFSI–LiTFSI (green dots, 7 mS cm^{-1} at 60 °C and 0.03 mS cm^{-1} at −30 °C) and DEMETFSI–LiTFSI (red dots, 7 mS cm^{-1} at 60 °C and 0.02 mS cm^{-1} at −30 °C). Thus, all the investigated samples reveal suitable conductivity for application in batteries only above room temperature. Fig. 1b reports the viscosity *versus* temperature plots and shows that the Pyr_{14}FSI–LiTFSI electrolyte (black dots, 13 mP s at 80 °C, 1573 mP s at −30 °C) is characterized by the lowest viscosity, followed by Pyr_{12O1}TFSI–LiTFSI (blue dots, 14 mP s at 80 °C, 5730 mP s at −30 °C). Instead, Pyr_{14}TFSI–

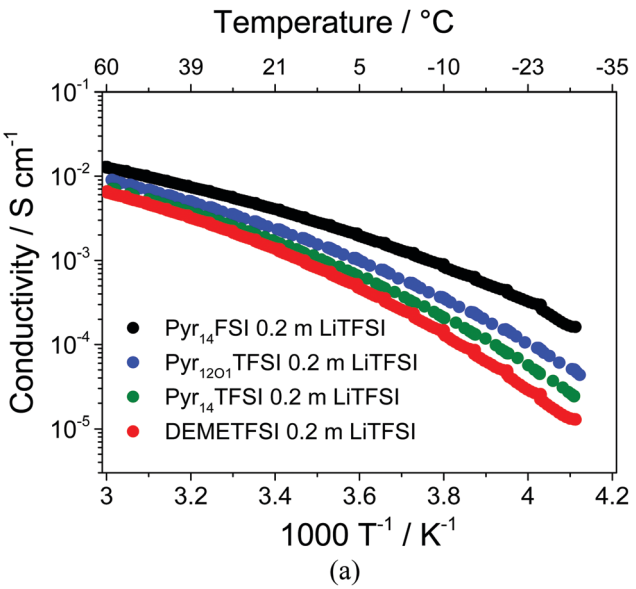

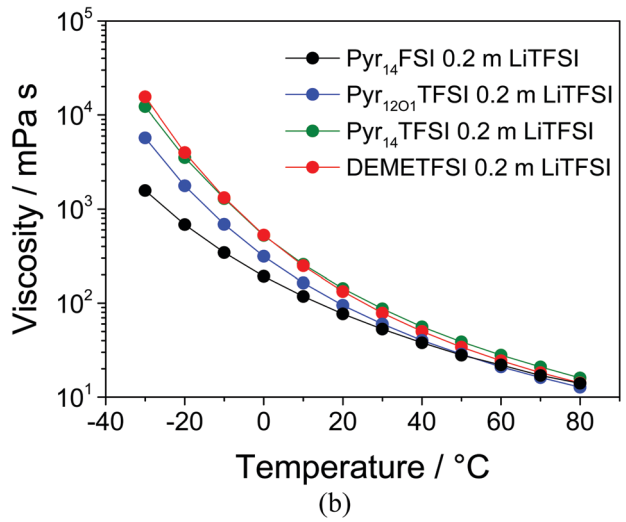

Fig. 1 (a) Conductivity and (b) viscosity Arrhenius plots of $Pyr_{14}TFSI$–LiTFSI (green dot), $Pyr_{14}FSI$–LiTFSI (black dot), $Pyr_{12O1}TFSI$–LiTFSI (blue dot), DEMETFSI–LiTFSI (red dot).

LiTFSI (green dots, 16 mP s at 80 °C, 12 250 mP s at −30 °C) and DEMETFSI–LiTFSI (red dots, 14 mP s at 80 °C, 15 565 mP s at −30 °C) exhibit the highest viscosity values.

The viscosity and the conductivity trends reported in Fig. 1 deviate from the linear behavior expected for an Arrhenius-type curve, but can be properly described by the Vogel–Tammann–Fulcher (VTF) model, in particular at low temperatures[6]>. The model is mathematically expressed by VTF eqn (1) for conductivity, and (2) for viscosity, with the introduction of the T_0 (K) correction parameter.

$$\sigma(T) = \sigma_\infty \exp\left(-\frac{E_{a\sigma}}{k_B(T - T_0)}\right) \quad (1)$$

$$\eta(T) = \eta_\infty \exp\left(-\frac{E_{a\eta}}{k_B(T - T_0)}\right) \quad (2)$$

This value, often referred to as zero configurational entropy and correlated to the glass transition temperature T_g (K) of each ionic liquid, is generally about 30 K lower than the T_g[6] >. The other parameters in eqn (1) and (2) are the ionic conductivity at infinite temperature σ_∞ (S cm^{-1}), the maximum dynamic viscosity η_∞ (mP s), the activation energy for ion conduction $E_{a\sigma}$ (eV), the dynamic viscosity activation energy $E_{a\eta}$ (eV) and the Boltzmann constant k_B (8.62×10^{-5} eV K^{-1}). Tables 1 and 2 report the results obtained by non-linear-least-square (NLLSQ) fits of conductivity and viscosity VTF curves, respectively, for $Pyr_{14}TFSI$–LiTFSI, $Pyr_{14}FSI$–LiTFSI, $Pyr_{12O1}TFSI$–LiTFSI, and DEMETFSI–LiTFSI electrolytes (see ESI†, Fig. S2, for the corresponding linearized VTF plots: a, c, e and g for conductivity and b, d, f and h for viscosity).[75,76]

The trends of Fig. 1b well agree with the Walden law, thus suggesting an ionic conductivity controlled by viscosity within the investigated temperature range and under operating conditions.[75] Previous papers have shown possible liquid–solid phase transition for $Pyr_{14}TFSI$–LiTFSI and $Pyr_{14}FSI$–LiTFSI by quenching the samples with liquid nitrogen[77,78] that is, however, not revealed by our experimental setup. In order to avoid possible drawbacks due to electrode and separator wetting and considering the conductivity and viscosity trends above, 40 °C

Table 1 Value of the ionic conductivity at infinite temperature, activation energy and T_0 obtained by the VTF fit of the conductivity plots

	σ_∞ [S cm^{-1}]	E_a [eV]	T_0 [K]
$Py_{14}FSI$ 0.2 m LiTFSI	0.6 ± 0.1	$5.9 \times 10^{-2} \pm 0.1 \times 10^{-2}$	159 ± 3
$Py_{14}TFSI$ 0.2 m LiTFSI	0.7 ± 0.1	$6.4 \times 10^{-2} \pm 0.1 \times 10^{-2}$	172 ± 3
$Py_{12O1}TFSI$ 0.2 m LiTFSI	0.7 ± 0.1	$6.1 \times 10^{-2} \pm 0.1 \times 10^{-2}$	170 ± 3
DEMETFSI 0.2 m LiTFSI	0.5 ± 0.1	$5.5 \times 10^{-2} \pm 0.1 \times 10^{-2}$	186 ± 3

Table 2 Value of the maximum dynamic viscosity, activation energy and T_0 obtained by the VTF fit of the viscosity plots

	η_∞ [mP s]	E_a [eV]	T_0 [K]
$Py_{14}FSI$ 0.2 m LiTFSI	0.31 ± 0.05	$6.84 \times 10^{-2} \pm 0.1 \times 10^{-2}$	154 ± 3
$Py_{14}TFSI$ 0.2 m LiTFSI	0.14 ± 0.03	$7.33 \times 10^{-2} \pm 0.1 \times 10^{-2}$	168 ± 3
$Py_{12O1}TFSI$ 0.2 m LiTFSI	0.18 ± 0.04	$6.84 \times 10^{-2} \pm 0.1 \times 10^{-2}$	167 ± 3
DEMETFSI 0.2 m LiTFSI	0.14 ± 0.03	$7.15 \times 10^{-2} \pm 0.1 \times 10^{-2}$	172 ± 3

was selected as the preferred temperature for testing the IL-based electrolytes in half and full-cell configurations.[76] The cyclic voltammetry (CV) scans of the cathodic region recorded with the investigated electrolytes in contact with composite carbon working electrodes are reported in Fig. 2a. The initial cycle evidences, for all electrolytes, the irreversible peak associated with the SEI formation at the carbon-based working electrode (Super C65). However, such a peak occurs at rather different potentials depending on the electrolyte composition, *i.e.*, at about 1.3 V *vs.* Li/Li^+ for the $Pyr_{14}FSI$–LiTFSI (black)[51] and 0.6 V *vs.* Li/Li^+ for $Pyr_{14}TFSI$–LiTFSI (green), $Pyr_{12O1}TFSI$–LiTFSI (blue) and DEMETFSI–LiTFSI (red).[79–81] The higher SEI formation potential observed for the former electrolyte may be ascribed to the FSI anion decomposition known to have enhanced film-forming ability compared to TFSI.[82] The second cycle, reported in the lower panel, reveals the exclusive presence of reversible peaks in the 0.0–0.2 V *vs.* Li/Li^+ region associated with the lithium uptake in the carbon working electrode,[83] thus suggesting the formation of a stable solid electrolyte interface (SEI) film with all the investigated electrolytes which prevents any further decomposition process during the following cycles.

The anodic stability of the electrolytes is evaluated by measuring the current evolution during a stepwise potential sweep, increasing by 0.1 V each one hour, (Fig. 2b). All the investigated electrolytes exhibit no current flow below 4.5 V *vs.* Li/Li^+. At higher potential values, *i.e.*, 4.6 V *vs.* Li/Li^+, the DEMETFSI–LiTFSI electrolyte (red line) shows negligible current flow, associated with side reactions, that slightly increases at 4.7–4.8 V *vs.* Li/Li^+, finally reaching about 10 μA cm^{-2} at 4.9 V *vs.* Li/Li^+, most likely due to the electrolyte decomposition. Instead, $Pyr_{12O1}TFSI$–LiTFSI (blue line) and $Pyr_{14}FSI$–LiTFSI (black line) show negligible current flow until 4.9 V *vs.* Li/Li^+, while at 5 V *vs.* Li/Li^+ a current flow of about 10 μA cm^{-2} can be noticed. Overall, $Pyr_{14}TFSI$–LiTFSI (green line) shows the best electrochemical stability, with only minor current flowing below 5.1 V *vs.* Li/Li^+. The inset of Fig. 2b, reporting the linear scan voltammetry (LSV) tests of the investigated electrolytes performed at a scan rate of 0.1 mV s^{-1}, well confirms the data obtained by the stepwise potential measurement. Indeed, the anodic stability of the investigated electrolytes may be summarized as the following: $Pyr_{14}TFSI$–LiTFSI (5.1 V *vs.* Li/Li^+); $Pyr_{14}FSI$–LiTFSI (4.8–4.9 V *vs.* Li/Li^+); $Pyr_{12O1}TFSI$–LiTFSI DEMETFSI–LiTFSI (4.8–4.9 V *vs.* Li/Li^+); DEMETFSI–LiTFSI (4.7 V *vs.* Li/Li^+). Fig. 2c reports the polarization *versus* time signatures of the stripping/deposition tests in symmetrical Li/electrolyte/Li cells used in order to determine the compatibility of the electrolytes against lithium metal under current flow. The cells employing DEMETFSI–LiTFSI (red), $Pyr_{12O1}TFSI$–LiTFSI (blue) and $Pyr_{14}FSI$–LiTFSI (black) electrolytes show a lithium stripping/deposition polarization stably limited to about 55, 45, and 15 mV, respectively, thus suggesting an optimized SEI formation at the lithium surface. The various resistance values may be attributed to different morphologies and compositions of the SEI formed at the lithium surface by changing the IL-electrolyte media. Instead, the cell using the $Pyr_{14}TFSI$–LiTFSI

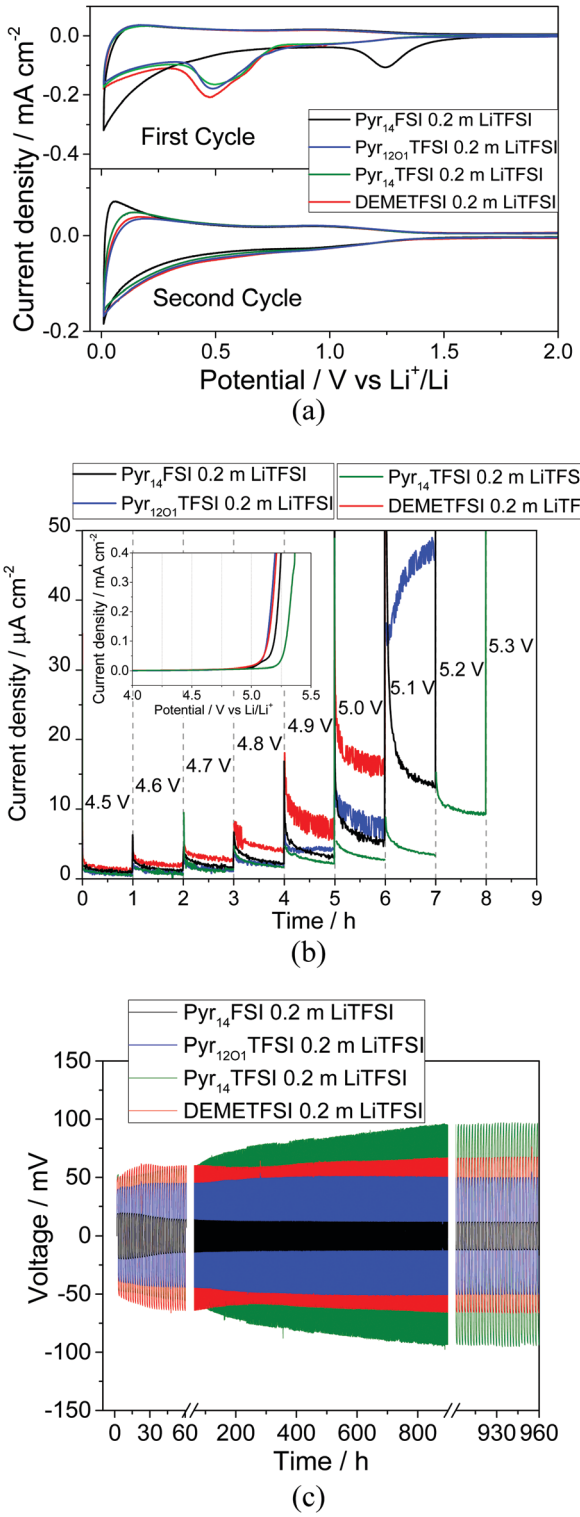

Fig. 2 (a) Cyclic voltammograms of Li/IL/Super-C65 cells recorded at a scan rate of 0.1 mV s^{-1} (first and second cycles). (b) Current *vs.* time profile of the Li/IL/Super-C65 cells subjected to a stepwise potential sweep (the inset shows the current *vs.* potential plot upon linear sweep voltammetry on Li/IL/Super-C65 cells) at a scan rate of 0.1 mV s^{-1}, (c) voltage *vs.* time plot recorded upon stripping/deposition measurements performed on asymmetrical Li/IL/Li cells at a current of 0.1 mA cm^{-2} and a deposition-stripping time of 1 h. $Pyr_{14}TFSI$–LiTFSI (green), $Pyr_{14}FSI$–LiTFSI (black), $Pyr_{12O1}TFSI$–LiTFSI (blue), DEMETFSI–LiTFSI (red) electrolytes. All measurements were performed at 40 °C.

electrolyte shows a polarization increasing up to 95 mV after 40 days (480 cycles, 960 h) most likely ascribed to the growth of the SEI layer. Previous works indicated the replacement of the lithium metal anode by a Li-alloying anode as a suitable pathway for solving this issue.[59] Remarkably, despite the mid-high temperature range (40 °C) used for stripping/deposition measurements, the cell stability extends over 480 cycles, *i.e.*, 40 days of continuous cell operation, thus suggesting enhanced characteristics of the lithium/IL-electrolyte interface.

The suitability of the IL-based electrolytes was further evaluated by galvanostatic cycling in Li//LFP cells. Fig. 3a shows the voltage signature during a steady state cycle of the cells employing the four investigated electrolytes at a specific current of 25 mA g^{-1} (corresponding to *ca.* C/7 rate) in the 2.2–4 V voltage range, performed at 40 °C. The voltage signatures reflect the typical flat voltage profile associated with the reversible insertion of lithium ions in the LFP olivine structure[11,84–86] with very low (dis-)charge polarization and only minor differences between the electrolytes (magnified in the inset of Fig. 3a). The highest reversible capacity (about 165 mA h g^{-1}, *i.e.*, 97% of the theoretical value) is shown by the cells employing Pyr_{12O1}TFSI–LiTFSI (blue line) and Pyr_{14}FSI–LiTFSI (black line), while a capacity of 161 mA h g^{-1} is shown by the cells employing Pyr_{14}TFSI–LiTFSI (green line) and DEMETFSI–LiTFSI (red line). The detailed evaluation of the average cell polarization reported in Fig. S3a (ESI†) shows a value of about 70 mV for the cell using Pyr_{14}FSI–LiTFSI, 100 mV for Pyr_{12O1}TFSI–LiTFSI, 110 mV for Pyr_{14}TFSI–LiTFSI and 120 mV for DEMETFSI–LiTFSI electrolytes. Increasing current leads to more marked differences in (dis-)charge polarization, as evidenced in Fig. 3b reporting the voltage signature of the 70th galvanostatic cycle performed at 250 mA g^{-1} (*ca.* 1.5C). The best performance is achieved by employing the Pyr_{14}FSI–LiTFSI electrolyte (Fig. 3b, black line) which retains 95% of the capacity upon a tenfold increase of current, *i.e.* from 25 mA g^{-1} (Fig. 3a) to 250 mA g^{-1} (Fig. 3b), with an average polarization of 230 mV (Fig. S3b, ESI†). Instead, the cell employing the Pyr_{12O1}TFSI–LiTFSI electrolyte (Fig. 3b, blue circles) can deliver at a higher current a capacity of 100 mA h g^{-1} with an average polarization of 430 mV (Fig. S3b, ESI†), while the cells employing the DEMETFSI–LiTFSI (Fig. 3b, red line) and Pyr_{14}TFSI–LiTFSI (Fig. 3b, green line) electrolytes deliver a capacity of about 65 mA h g^{-1} and 70 mA h g^{-1} with an average polarization of 450 mV and 480 mV, respectively (Fig. S3b, ESI†). The polarization of the cells employing various IL-based electrolytes appears to be in line with the conductivity and viscosity trends as well as the lithium/electrolyte interface stability. However, the cell using Py_{14}TFSI–LiTFSI shows an increased polarization when the current is lowered back to 25 mA g^{-1} at the 90th cycle (Fig. S3c, ESI†) compared to the initial cycles (compare with Fig. S3c, ESI†). This is certainly due to the progressive growth of a more resistive SEI at the lithium metal anode. This trend matches the one already observed by stripping-deposition measurements in lithium symmetrical cells reported in Fig. 2c.

Fig. 3c, overlapping the cycling trends at increasing currents of the lithium cells above discussed (see the corresponding voltage profiles in Fig. 3a and b), shows only minor capacity fading with a retention of about 95% after 100 cycles for the cell

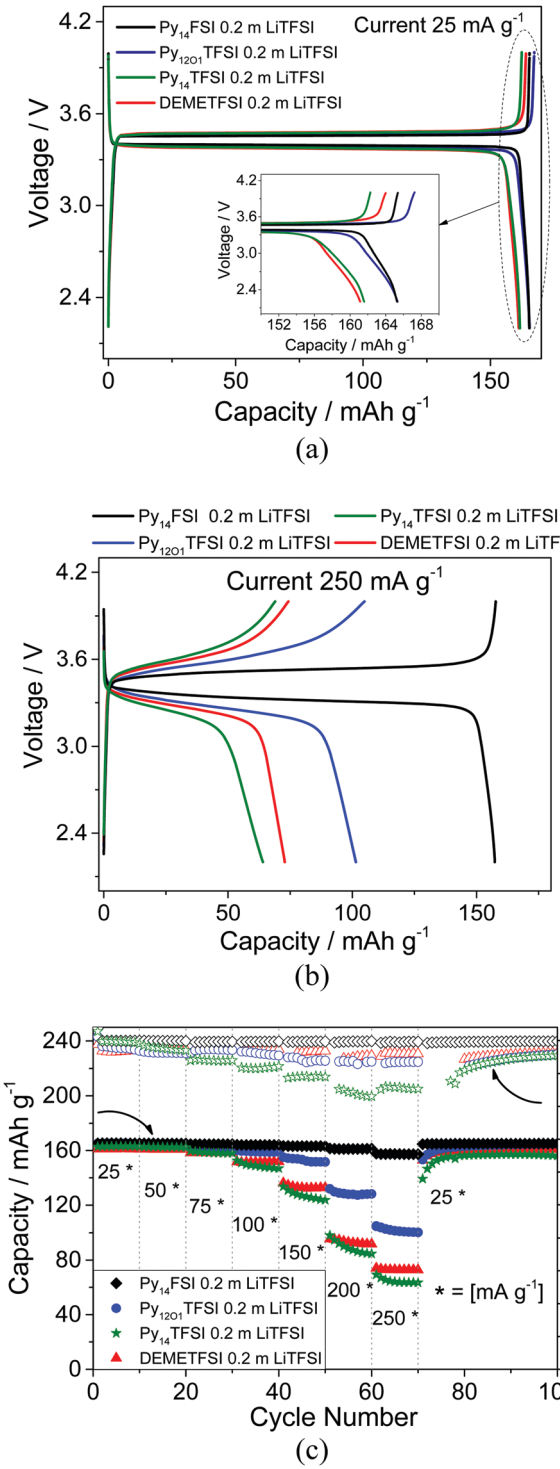

Fig. 3 Steady state voltage signatures of Li/IL/LFP cells galvanostatically cycled at (a) 25 mA g^{-1} (0.12 mA cm^{-2}) and (b) 250 mA g^{-1} (1.2 mA cm^{-2}). (c) Cycling trend and columbic efficiency of the Li/IL/LFP cells at increasing currents, *i.e.*, 25, 50, 75, 100, 150, 200 and 250 mA g^{-1} (0.12, 0.24, 0.36, 0.48, 0.72, 0.96, and 1.2 mA cm^{-2}, respectively). Voltage cut-offs were 2.2 and 4 V. Pyr_{14}TFSI–LiTFSI (green), Pyr_{14}FSI–LiTFSI (black), Pyr_{12O1}TFSI–LiTFSI (blue), DEMETFSI–LiTFSI (red). All measurements were performed at 40 °C.

employing Pyr_{14}TFSI–LiTFSI. Remarkably, the cells using Pyr_{12O1}TFSI–LiTFSI, Pyr_{14}FSI–LiTFSI and DEMETFSI–LiTFSI electrolytes evidence negligible capacity fading and retention higher than 99%. Fig. 3c shows the good rate capability for all the investigated electrolytes and, in particular, the excellent response of Pyr_{14}FSI–LiTFSI due to its higher ionic conductivity and lower viscosity. Furthermore, the cell employing this electrolyte shows a very high coulombic efficiency (about 99.9%) with respect to those using Pyr_{12O1}TFSI–LiTFSI and DEMETFSI–LiTFSI (about 98%). Instead, Pyr_{14}TFSI–LiTFSI electrolyte shows a high coulombic efficiency (99.9%) only during the initial cycling stage at a lower current (25 mA g^{-1}) and remarkably lower efficiency (92%) at the higher current (250 mA g^{-1}). The coulombic efficiency is calculated as the ratio of the electricity delivered and accumulated in the battery through the faradaic processes, involving electron transfer reactions at the electrode/electrolyte interfaces, in the course of lithium (de)insertion at the cathode and (de)alloying at the anode. Capacitive effects, on the other hand, are considered negligible due to the very limited electrode surface areas.[87] Hence, the lower efficiency of the latter cell by increasing the C-rate may be attributed to kinetic effects of the current, promoted by the high viscosity of the electrolyte (Fig. 1b), and favoring the irreversible parasitic reactions with respect to the reversible charge transfer process. Furthermore, the increased cell polarization upon charging at high C-rates, which results in higher and lower voltages experienced by the electrolyte at, respectively, the positive and negative electrodes, may indeed favor the occurrence of irreversible parasitic reactions, resulting in decreased efficiency.

Based on the above reported results, Pyr_{14}FSI–LiTFSI was selected as the electrolyte of choice for the realization of the lithium-ion cell prototype employing a Sn–C nanocomposite anode.[68,71] Prior to assembling the full cell, the Sn–C electrode was pre-lithiated in order to eliminate its first cycle irreversible capacity (see the Experimental section), thus allowing proper cell balancing and operation[73,8]>. The voltage profile of the Li/Pyr_{14}FSI–LiTFSI/Sn–C half-cell (Fig. S4a in ESI†) shows the typical signature ascribed to the reversible alloying of lithium with tin.[18,68,89] The Li/Pyr_{14}FSI–LiTFSI/Sn–C cell delivers a capacity of 400 mA h g^{-1} over 400 cycles, with a columbic efficiency as high as 99.9% (Fig. S4b in ESI†) and a very good rate capability (Fig. S4c and d in ESI†). This performance confirms Sn–C as a suitable anode for application in efficient and effective lithium ion cells as well as the remarkable SEI forming ability of the electrolyte employing the FSI^- anion. The nature and composition of the SEI formed at the alloy anode surface in IL-based electrolytes has been clarified by a recent work.[61] The study reveals that the FSI^- anion can decompose during the reduction process at the alloy anode (S–F bond breaking). This process leads to the formation of SO_2 and LiO at the anode/electrolyte interface and consolidation of the SEI layer by adherent compounds such as LiF, LiO, LiOH and Li_2SO_4. Fig. 4a shows the steady state voltage signature of the Sn–C/Pyr_{14}FSI–LiTFSI/$LiFePO_4$ cell at currents of 25, 75, 150 and 250 mA g^{-1} (all specific values of the lithium-ion cell refer to the active cathode material mass). The voltage shape reflects the combination of the flat profile of the LFP cathode and the sloping profile of the Sn–C anode, following the overall electrochemical process:

$$Li_xSn\text{–}C + LiFePO_4 \leftrightarrow Li_{x+y}Sn\text{–}C + Li_{(1-y)}FePO_4.$$

The cell delivers a specific capacity as high as 160 mA h g^{-1} at a lower current (25 mA g^{-1}) and a still satisfactory value of 105 mA h g^{-1} at a higher one (250 mA g^{-1}), with rather remarkable rate capability, cycling trend and coulombic efficiency (Fig. 4b). The cycling test of the Li-ion cell at a current density of 100 mA g^{-1} (Fig. 4c) reveals a reversible capacity of 150 mA g^{-1} with negligible capacity fading, columbic efficiency higher than 99.9%, resulting in a cycle life extending over 1000 cycles, and an average working voltage change by cycles limited to about 100 mV (Fig. 4d). A further long-term test, aiming to determine the cell cycle-life, was performed using a test procedure in which low (25 mA g^{-1}) and high current (500 mA g^{-1}) cycles were continuously repeated (Fig. 4e). Although subjected to these stressful conditions, the cell could reversibly deliver specific capacity well over 80 mA h g^{-1} at the highest current, fully recovering to its pristine value of 160 mA h g^{-1} at a lower current. Overall, the cell showed a capacity retention of about 98% over more than 2000 cycles and columbic efficiency close to 100%. Fig. 4f shows the comparison of the voltage profiles during the 2nd and 2018th low current cycles and the 20th and 2030th high current cycles. The figure remarkably reveals a working voltage change limited to about 100 mV between the initial and the final cycles. Based on the cycling response at various current rates, we determined the theoretical energy and power densities of the cell as referred to the cathode weight. Furthermore, the system reveals good electrochemical performance even at the lowest temperature, *i.e.* 20 °C, as evidenced by the cycling test reported in Fig. S5 in the ESI.† The results reveal at 25 mA g^{-1} a capacity of 150 mA h g^{-1}, which is slightly lower than that delivered at 40 °C, but with a comparably stable trend, high efficiency and low polarization. However, a lower capacity and higher polarization are observed by raising the current, as indeed expected for the lower ionic conductivity (*i.e.* higher viscosity) of the electrolyte at 20 °C (see Fig. 1).

The plot of Fig. S6 (ESI†) reports the energy density (left *y*-axis) and the power density (right *y*-axis) of the Sn–C/Pyr_{14}FSI–LiTFSI/LFP lithium-ion cell reported as function of the operating current. The cell reaches maximum values of specific energy and power densities of 460 W h kg^{-1} and 1400 W kg^{-1}, respectively, that may likely reflect into practical values well suited for efficient and high performance energy storage applications. The relevant performance of the Pyr_{14}FSI–LiTFSI with respect to the other investigated IL solutions is further evidenced by the comparison of the Sn–C/LFP cell performances using the various electrolytes, reported in Fig. S7 in the ESI.† The figure reveals higher delivered capacity and columbic efficiency for the cell employing the Pyr_{14}FSI–LiTFSI electrolyte.

The exceptional performance of the Sn–C/Pyr_{14}FSI–LiTFSI/$LiFePO_4$ cell may be clarified by the evolution of the cell impedance upon cycling (Fig. 5a), obtained by analyzing the EIS response reported in Fig. S8a (ESI†) together with the equivalent circuit (Fig. S8b, ESI†) used for the nonlinear least

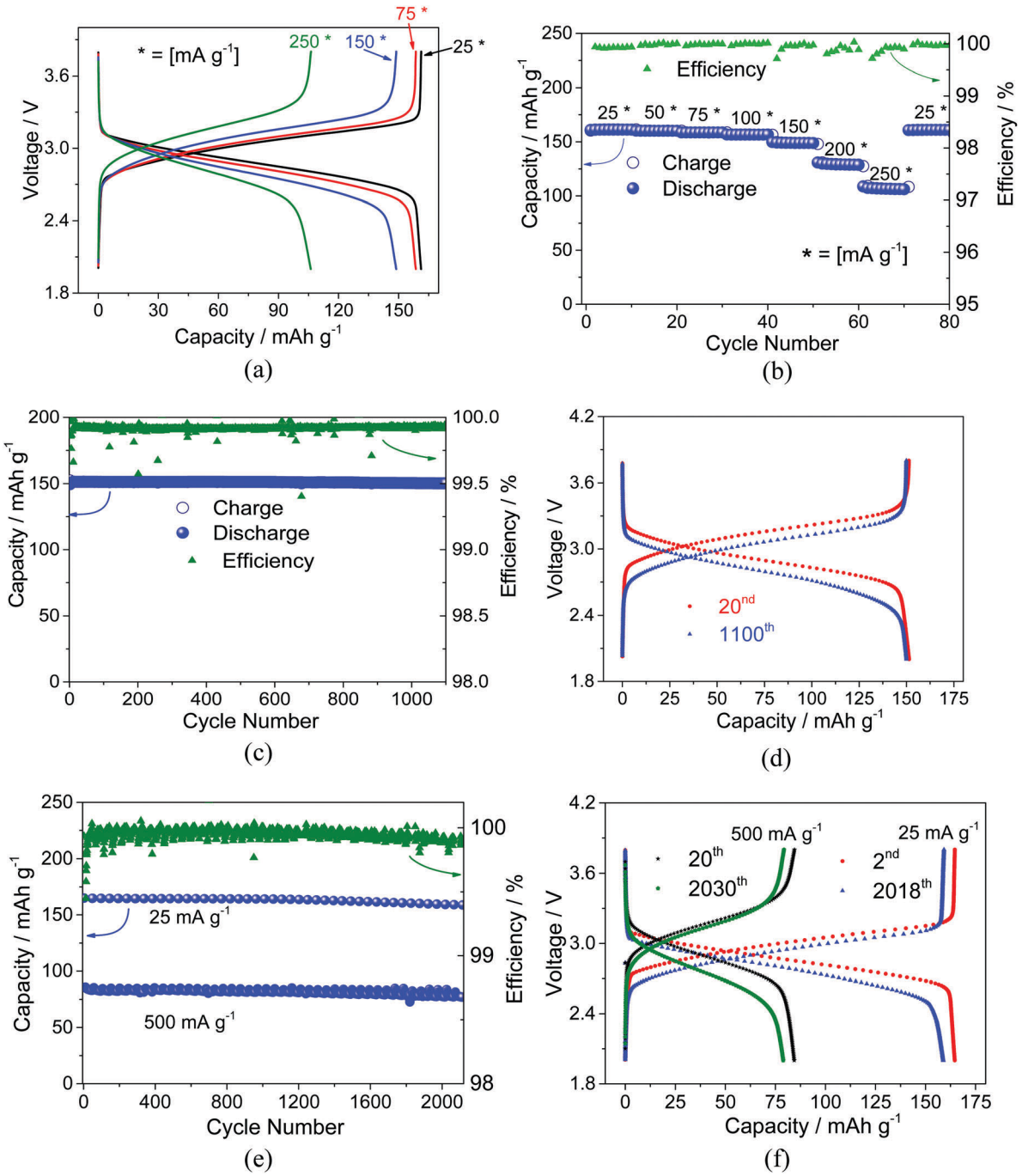

Fig. 4 (a) Selected steady state voltage signatures and (b) cycling behavior with the columbic efficiency of the Sn–C/Pyr_{14}FSI–LiTFSI/LFP cell galvanostatically measured at increasing currents, *i.e.*, 25, 50, 75, 100, 150, 200 and 250 mA g^{-1} (0.12, 0.24, 0.36, 0.48, 0.72, 0.96, and 1.2 mA cm^{-2}, respectively). (c) Columbic efficiency and (d) steady state voltage signatures of the Sn–C/Pyr_{14}FSI–LiTFSI/LFP cell in a long-term galvanostatic cycling test at 100 mA g^{-1} (1.2 mA cm^{-2}). (e) Columbic efficiency and (f) steady state voltage signatures of the Sn–C/Pyr_{14}FSI–LiTFSI/LFP cell galvanostatically cycled at different currents, *i.e.*, 25 and 500 mA g^{-1} (0.12 and 2.4 mA cm^{-2}, respectively). All measurements were performed at 40 °C and a cut off voltage of 2–3.8 V.

Q7 square (NLLSQ) fit procedure[90,9]>. The cell shows a very low overall cell internal resistance at the open circuit (OCV, 16 Ω), slightly increasing during the initial 10 cycles due to SEI film formation and consolidation at the electrode surfaces,[92,93] and finally stabilizing to about 25 Ω over 200 cycles, with only small changes considered within the experimental error of the measurement. Accordingly, the SEI film formation at the electrode surface is completed upon 10 charge/discharge cycles. Further proof of the cell interface stability is given by *ex situ* SEM micrographs of Sn–C (Fig. 5b) and LFP (Fig. 5c) electrodes, obtained after cell assembly (OCV), upon 10 cycles and 200 cycles. The figures clearly reveal negligible morphological changes for the two materials upon cycling, thus further accounting for the extended stability of the electrode/electrolyte interface.

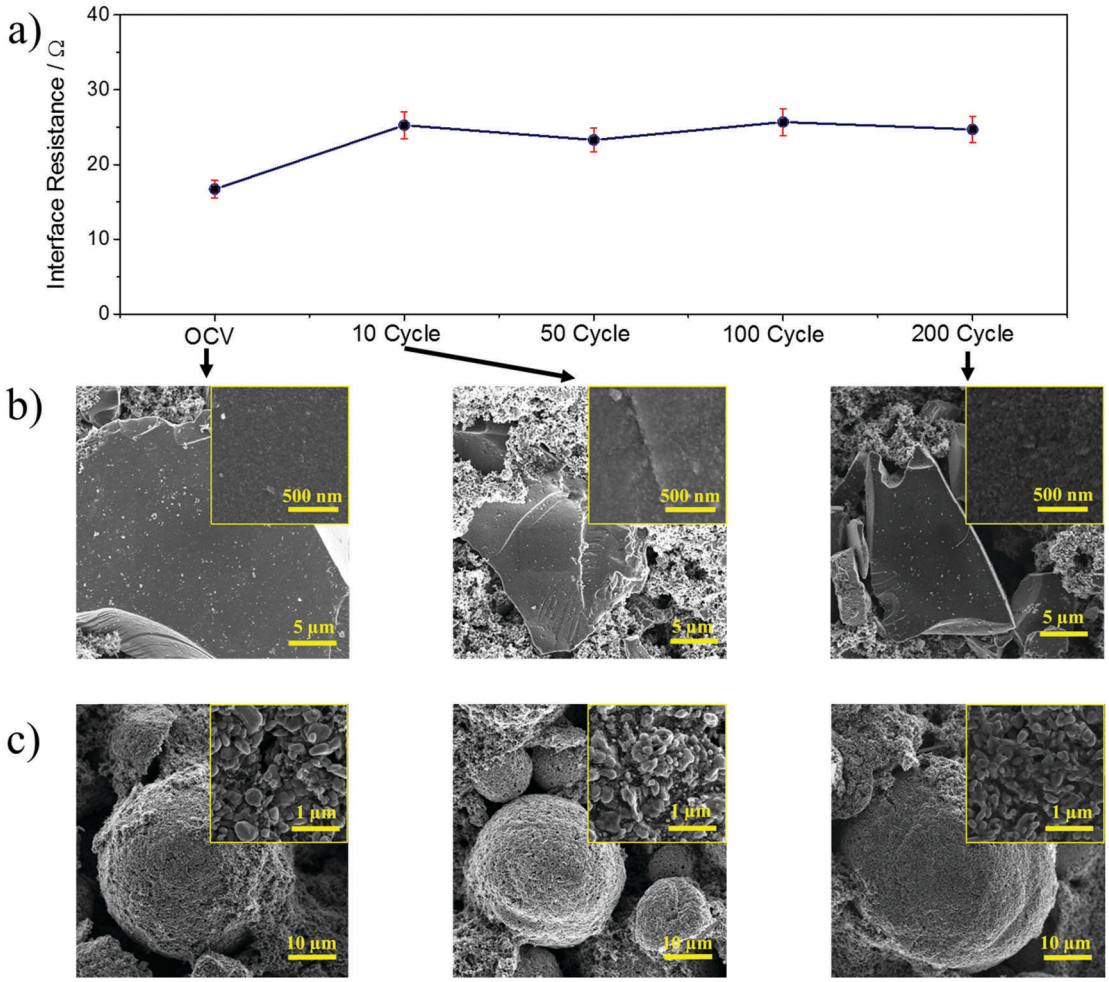

Q8 Fig. 5 (a) Evolution of the interface resistance of the Sn–C/Pyr_{14}FSI–LiTFSI/LFP cell upon cycling. (b and c) *Ex situ* SEM images of the electrode materials (Sn–C and LFP) subjected to galvanostatic cycling.

Conclusions

We investigated an enhanced class of ionic liquid-based electrolytes for application in advanced, long life and safe lithium ion batteries. Basically, all the investigated electrolytes have shown suitable ionic conductivity and excellent electrochemical stability. The Vogel–Tammann–Fulcher (VTF) model well represented the behavior of conductivity and viscosity of the electrolytes, thus leading to parameters calculated by linear plots in good agreement with the Walden law within the explored temperature range. In particular, Pyr_{14}FSI–LiTFSI revealed the highest ionic conductivity, lowest viscosity, most suitable lithium/electrolyte interface and remarkably low polarization under current flow. These characteristics are reflected in the outstanding performance of the Sn–C/Pyr_{14}FSI–LiTFSI/LFP lithium-ion cell, delivering a maximum capacity of 160 mA h g^{-1} at an average working voltage of 3 V with a columbic efficiency higher than 99.9% over more than 2000 charge/discharge cycles. Such a performance is achieved because of the exceptionally stable cell impedance upon cycling, as demonstrated by *in situ* EIS measurements and *ex situ* SEM characterization. The lithium-ion cell here presented is indeed extremely appealing as a safe energy storage system for a wide range of applications, such as modern electronic devices and electric vehicles.

Acknowledgements

The authors acknowledge BMW AG for the financial support. J. H. thanks the collaboration project ''Accordo di Collaborazione Quadro 2015'' between University of Ferrara (Department of Chemical and Pharmaceutical Sciences) and Sapienza University of Rome (Chemistry Department). The authors would like to thank Dr Andrea Balducci and Thomas Vogl for useful discussion on viscosity measurements.

References

1 B. Scrosati and J. Garche, *J. Power Sources*, 2010, **195**, 2419–2430.
2 J. Y. Yong, V. K. Ramachandaramurthy, K. M. Tan and N. Mithulananthan, *Renewable Sustainable Energy Rev.*, 2015, **49**, 365–385.

3 F. Orecchini, A. Santiangeli and A. Dell-Era, *Lithium-Ion Batteries*, 2014, 205–248.
4 M. S. Whittingham, *Chem. Rev.*, 2014, **114**, 11414–11443.
5 C. L. Campion, W. Li and B. L. Lucht, *J. Electrochem. Soc.*, 2005, **152**, A2327.
6 S. E. Sloop, J. B. Kerr and K. Kinoshita, *J. Power Sources*, 2003, **119–121**, 330–337.
7 P. G. Balakrishnan, R. Ramesh and T. Prem Kumar, *J. Power Sources*, 2006, **155**, 401–414.
8 M. Armand, F. Endres, D. R. MacFarlane, H. Ohno and B. Scrosati, *Nat. Mater.*, 2009, **8**, 621–629.
9 S. Abada, G. Marlair, A. Lecocq, M. Petit, V. Sauvant-Moynot and F. Huet, *J. Power Sources*, 2016, **306**, 178–192.
10 B. Scrosati, *Lithium Batteries*, John Wiley & Sons, Inc., Hoboken, NJ, USA, 2013, pp. 21–38.
11 A. K. Padhi, K. S. Nanjundaswamy and J. B. Goodenough, *J. Electrochem. Soc.*, 1997, **144**, 1188–1194.
12 Y. Wang, P. He and H. Zhou, *Energy Environ. Sci.*, 2011, **4**, 805–817.
13 P. G. Bruce, B. Scrosati and J.-M. Tarascon, *Angew. Chem., Int. Ed.*, 2008, **47**, 2930–2946.
14 R. A. Huggins, *J. Power Sources*, 1999, **81–82**, 13–19.
15 W.-J. Zhang, *J. Power Sources*, 2011, **196**, 13–24.
16 G. G. Graf, *Ullmann's Encyclopedia of Industrial Chemistry*, Wiley-VCH Verlag GmbH & Co. KGaA, Weinheim, Germany, 2000.
17 D. Deng, M. G. Kim, J. Y. Lee and J. Cho, *Energy Environ. Sci.*, 2009, **2**, 818.
18 M. N. Obrovac and V. L. Chevrier, *Chem. Rev.*, 2014, **114**, 11444–11502.
19 U. Kasavajjula, C. Wang and A. J. Appleby, *J. Power Sources*, 2007, **163**, 1003–1039.
20 E. Kwon, H.-S. Lim, Y.-K. Sun and K.-D. Suh, *Solid State Ionics*, 2013, **237**, 28–33.
21 K. Shin, D.-J. Park, H.-S. Lim, Y.-K. Sun and K.-D. Suh, *Electrochim. Acta*, 2011, **58**, 578–582.
22 A. Birrozzi, F. Maroni, R. Raccichini, R. Tossici, R. Marassi and F. Nobili, *J. Power Sources*, 2015, **294**, 248–253.
23 R. Kataoka, T. Mukai, A. Yoshizawa and T. Sakai, *J. Electrochem. Soc.*, 2013, **160**, A1684–A1689.
24 G. A. Elia, S. Panero, A. Savoini, B. Scrosati and J. Hassoun, *Electrochim. Acta*, 2013, **90**, 690–694.
25 J. Hassoun, G. A. Elia, S. Panero and B. Scrosati, *J. Power Sources*, 2011, **196**, 7767–7770.
26 C. Chae, H.-J. Noh, J. K. Lee, B. Scrosati and Y.-K. Sun, *Adv. Funct. Mater.*, 2014, **24**, 3036–3042.
27 R. Elazari, G. Salitra, G. Gershinsky, A. Garsuch, A. Panchenko and D. Aurbach, *Electrochem. Commun.*, 2012, **14**, 21–24.
28 L. Ji, H. Zheng, A. Ismach, Z. Tan, S. Xun, E. Lin, V. Battaglia, V. Srinivasan and Y. Zhang, *Nano Energy*, 2012, **1**, 164–171.
29 K. Eom, T. Joshi, A. Bordes, I. Do and T. F. Fuller, *J. Power Sources*, 2014, **249**, 118–124.
30 T. A. Yersak, S.-B. Son, J. S. Cho, S.-S. Suh, Y.-U. Kim, J.-T. Moon, K. H. Oh and S.-H. Lee, *J. Electrochem. Soc.*, 2013, **160**, A1497–A1501.
31 J. S. Thorne, R. J. Sanderson, J. R. Dahn and R. a. Dunlap, *J. Electrochem. Soc.*, 2010, **157**, A1085.
32 A. D. W. Todd, R. E. Mar and J. R. Dahn, *J. Electrochem. Soc.*, 2007, **154**, A597.
33 K. N. Marsh, J. A. Boxall and R. Lichtenthaler, *Fluid Phase Equilib.*, 2004, **219**, 93–98.
34 D. R. MacFarlane, M. Forsyth, P. C. Howlett, M. Kar, S. Passerini, J. M. Pringle, H. Ohno, M. Watanabe, F. Yan, W. Zheng, S. Zhang and J. Zhang, *Nat. Rev. Mater.*, 2016, **1**, 15005.
35 G. B. Appetecchi, M. Montanino and S. Passerini, *ACS Symp. Ser.*, 2012, **1117**, 67–128.
36 G. G. Eshetu, S. Grugeon, H. Kim, S. Jeong, L. Wu, G. Gachot, S. Laruelle, M. Armand and S. Passerini, *ChemSusChem*, 2016, **9**, 462–471.
37 Y. Chen, X. Zhang, D. Zhang, P. Yu and Y. Ma, *Carbon*, 2011, **49**, 573–580.
38 B. Xu, F. Wu, R. Chen, G. Cao, S. Chen and Y. Yang, *J. Power Sources*, 2010, **195**, 2118–2124.
39 F. Pettersson, J. Keskinen, T. Remonen, L. von Hertzen, E. Jansson, K. Tappura, Y. Zhang, C.-E. Wilén and R. Österbacka, *J. Power Sources*, 2014, **271**, 298–304.
40 T. Yamamoto, T. Nohira, R. Hagiwara, A. Fukunaga, S. Sakai, K. Nitta and S. Inazawa, *J. Power Sources*, 2012, **217**, 479–484.
41 I. Hasa, S. Passerini and J. Hassoun, *J. Power Sources*, 2016, **303**, 203–207.
42 D. Monti, E. Jónsson, M. R. Palacín and P. Johansson, *J. Power Sources*, 2014, **245**, 630–636.
43 S. Menne, M. Schroeder, T. Vogl and A. Balducci, *J. Power Sources*, 2014, **266**, 208–212.
44 S. Menne, T. Vogl and A. Balducci, *Chem. Commun.*, 2015, **51**, 3656–3659.
45 P. Reale, A. Fernicola and B. Scrosati, *J. Power Sources*, 2009, **194**, 182–189.
46 M. Montanino, M. Moreno, M. Carewska, G. Maresca, E. Simonetti, R. Lo Presti, F. Alessandrini and G. B. Appetecchi, *J. Power Sources*, 2014, **269**, 608–615.
47 G. A. Elia, R. Bernhard and J. Hassoun, *RSC Adv.*, 2015, **5**, 21360–21365.
48 M. Agostini, U. Ulissi, D. Di Lecce, Y. Ahiara, S. Ito and J. Hassoun, *Energy Technol.*, 2015, **3**, 632–637.
49 D. Di Lecce, S. Brutti, S. Panero and J. Hassoun, *Mater. Lett.*, 2015, **139**, 329–332.
50 M. Nádherná, J. Reiter, J. Moškon and R. Dominko, *J. Power Sources*, 2011, **196**, 7700–7706.
51 J. Reiter, M. Nádherná and R. Dominko, *J. Power Sources*, 2012, **205**, 402–407.
52 L. G. Chagas, D. Buchholz, L. Wu, B. Vortmann and S. Passerini, *J. Power Sources*, 2014, **247**, 377–383.
53 J.-K. Kim, F. Mueller, H. Kim, S. Jeong, J.-S. Park, S. Passerini and Y. Kim, *ChemSusChem*, 2016, **9**, 42–49.
54 P. Wang, S. M. Zakeeruddin, P. Comte, I. Exnar and M. Grätzel, *J. Am. Chem. Soc.*, 2003, **125**, 1166–1167.
55 A. I. Bhatt, A. S. Best, J. Huang and A. F. Hollenkamp, *J. Electrochem. Soc.*, 2010, **157**, A66.

56 V. Borgel, E. Markevich, D. Aurbach, G. Semrau and M. Schmidt, *J. Power Sources*, 2009, **189**, 331–336.

57 E. Paillard, Q. Zhou, W. a. Henderson, G. B. Appetecchi, M. Montanino and S. Passerini, *J. Electrochem. Soc.*, 2009, **156**, A891.

58 J. Mun, T. Yim, S. Jurng, J. H. Park, S. Y. Lee, J. H. Ryu, Y. G. Kim and S. M. Oh, *Electrochem. Commun.*, 2011, **13**, 1256–1259.

59 G. A. Elia, U. Ulissi, F. Mueller, J. Reiter, N. Tsiouvaras, Y.-K. Sun, B. Scrosati, S. Passerini and J. Hassoun, *Chem. – Eur. J.*, 2016, **22**, 6808–6814.

60 H. Ohno, M. Yoshizawa-Fujita, K. Fujita and Y. Fukaya, *Electrochemical Aspects of Ionic Liquids*, John Wiley & Sons, Inc., Hoboken, NJ, USA, NJ, USA, 2011.

61 D. M. Piper, T. Evans, K. Leung, T. Watkins, J. Olson, S. C. Kim, S. S. Han, V. Bhat, K. H. Oh, D. A. Buttry and S.-H. Lee, *Nat. Commun.*, 2015, **6**, 6230.

62 E. E. Paillard, Q. Zhou, W. Henderson, G. B. Appetecchi, M. Montanino and S. Passerini, *ECS Trans.*, 2009, **16**, 51–57.

63 H. Matsumoto, H. Sakaebe, K. Tatsumi, M. Kikuta, E. Ishiko and M. Kono, *J. Power Sources*, 2006, **160**, 1308–1313.

64 J. Reiter, E. Paillard, L. Grande, M. Winter and S. Passerini, *Electrochim. Acta*, 2013, **91**, 101–107.

65 H. Matsumoto, H. Sakaebe and K. Tatsumi, *ECS Trans.*, 2009, 59–66.

66 M. L. P. Le, N. A. Tran, H. P. K. Ngo, T. G. Nguyen and V. M. Tran, *J. Solution Chem.*, 2015, **44**, 2332–2343.

67 T. Sato, T. Maruo, S. Marukane and K. Takagi, *J. Power Sources*, 2004, **138**, 253–261.

68 J. Hassoun, G. G. Derrien, S. Panero and B. Scrosati, *Adv. Mater.*, 2008, **20**, 3169–3175.

Q9 69 A. E. Visser, N. J. Bridges and R. D. Rogers, *Ionic Liq.*, 2012.

70 N. De Vos, C. Maton and C. V. Stevens, *ChemElectroChem*, 2014, **1**, 1258–1270.

71 G. Derrien, J. Hassoun, S. Panero and B. Scrosati, *Adv. Mater.*, 2007, **19**, 2336–2340.

72 S. Brutti, J. Hassoun, B. Scrosati, C.-Y. Lin, H. Wu and H.-W. Hsieh, *J. Power Sources*, 2012, **217**, 72–76.

73 J. Hassoun, K.-S. Lee, Y.-K. Sun and B. Scrosati, *J. Am. Chem. Soc.*, 2011, **133**, 3139–3143.

74 G. A. Elia, D. Bresser, J. Reiter, P. Oberhumer, Y.-K. Sun, B. Scrosati, S. Passerini and J. Hassoun, *ACS Appl. Mater. Interfaces*, 2015, **7**, 22638–22643.

75 C. Schreiner, S. Zugmann, R. Hartl and H. J. Gores, *J. Chem. Eng. Data*, 2010, **55**, 1784–1788.

76 J. Pires, L. Timperman, J. Jacquemin, A. Balducci and M. Anouti, *J. Chem. Thermodyn.*, 2013, **59**, 10–19.

77 G. B. Appetecchi, M. Montanino, M. Carewska, M. Moreno, F. Alessandrini and S. Passerini, *Electrochim. Acta*, 2011, **56**, 1300–1307.

78 W. A. Henderson and S. Passerini, *Chem. Mater.*, 2004, **16**, 2881–2885.

79 C. C. Nguyen and S. W. Song, *Electrochem. Commun.*, 2010, **12**, 1593–1595.

80 A. M. Andersson and K. Edström, *J. Electrochem. Soc.*, 2001, **148**, A1100.

81 D. Aurbach, *J. Power Sources*, 2000, **89**, 206–218.

82 L. Grande, J. von Zamory, S. L. Koch, J. Kalhoff, E. Paillard and S. Passerini, *ACS Appl. Mater. Interfaces*, 2015, **7**, 5950–5958.

83 H. Zheng, Q. Qu, L. Zhang, G. Liu and V. S. Battaglia, *RSC Adv.*, 2012, **2**, 4904.

84 B. W. Zewde, G. A. Elia, S. Admassie, J. Zimmermann, M. Hagemann, C. S. Isfort, B. Scrosati and J. Hassoun, *Solid State Ionics*, 2014, **268**, 174–178.

85 C. Masquelier and L. Croguennec, *Chem. Rev.*, 2013, **113**, 6552–6591.

86 M. S. Whittingham, *Chem. Rev.*, 2004, **104**, 4271–4301.

87 N. Böckenfeld, T. Placke, M. Winter, S. Passerini and A. Balducci, *Electrochim. Acta*, 2012, **76**, 130–136.

88 G. A. Elia, J. Wang, D. Bresser, J. Li, B. Scrosati, S. Passerini and J. Hassoun, *ACS Appl. Mater. Interfaces*, 2014, **6**, 12956–12961. Q10

89 S. D. Beattie, T. Hatchard, A. Bonakdarpour, K. C. Hewitt and J. R. Dahn, *J. Electrochem. Soc.*, 2003, **150**, A701.

90 B. Boukamp, *Solid State Ionics*, 1986, **18–19**, 136–140.

91 B. Boukamp, *Solid State Ionics*, 1986, **20**, 31–44.

92 A. Lewandowski and A. Świderska-Mocek, *J. Power Sources*, 2009, **194**, 601–609.

93 M. Broussely, P. Biensan, F. Bonhomme, P. Blanchard, S. Herreyre, K. Nechev and R. J. Staniewicz, *J. Power Sources*, 2005, **146**, 90–96.